arXiv:1603.02941v1 [cond-mat.mes-hall] 9 Mar 2016

Electron-Hole Asymmetry in the Electron-phonon Coupling in Top-gated Phosphorene Transistor

Biswanath Chakraborty,[†,¶] Satyendra Nath Gupta,[†,¶] Anjali Singh,[‡] Manabendra Kuiri,[†] Chandan Kumar,[†] D. V. S. Muthu,[†] Anindya Das,[†] U. V. Waghmare,[‡] and A. K. Sood[*,†]

Department of Physics, Indian Institute of Science, Bangalore 560012, India, and Theoretical Sciences Unit, Jawaharlal Nehru Centre for Advanced Scientific Research, Bangalore-560064, India

E-mail: asood@physics.iisc.ernet.in

KEYWORDS: phosphorene, phonon, Raman spectroscopy, electron-phonon coupling

March 10, 2016

Abstract

Using in-situ Raman scattering from phosphorene channel in an electrochemically top-gated field effect transistor, we show that its phonons with A_g symmetry depend much more strongly on concentration of electrons than that of holes, while the phonons with B_g symmetry are insensitive to doping. With first-principles theoretical analysis, we show that the observed electon-hole asymmetry arises from the radically different constitution of its conduction and valence bands involving π and σ bonding states respectively, whose symmetry permits coupling with only the phonons that preserve the lattice symmetry. Thus, Raman spectroscopy is

[*]To whom correspondence should be addressed

[†]Department of Physics, Indian Institute of Science, Bangalore 560012, India

[‡]Theoretical Sciences Unit, Jawaharlal Nehru Centre for Advanced Scientific Research, Bangalore-560064, India

[¶]Contributed equally to this work

a non-invasive tool for measuring electron concentration in phosphorene-based nanoelectronic devices.

Introduction

A few layer Black Phosphorus (BP) is a relatively new member of the family of 2D nanosystems with unique properties. Unlike gapless graphene, black phosphorus is a direct band gap material with gap ranging from 0.3 eV in bulk to 2 eV in monolayer,[1–7] covering a wide range of electromagnetic spectrum. This is again distinctive from transition metal dichalcogenides (TMD) which exhibit a direct band gap of $\sim$ 1 to 2 eV only in their monolayer form. The narrow band gap of BP (in few layer form) bridges the gap between the zero gap graphene and large band gap TMDs, thus making BP a suitable candidate for near and mid infrared optics.[8] For possible applications in electronic devices, black phosphorus offers a good possibility with mobilitiy of $\sim$ 1000 cm^2/V-sec at room temperature and On-Off ratio of $\sim 10^5$ with excellent current saturation characteristics.[9]

Phosphorene (as monolayer BP is referred to) lattice structure is a 2-D puckered network (Figure 1a) formed by phosphorus atoms with each atom covalently bonded to three neighbouring atoms. An unique feature of black phosphorus is its in-plane anisotropy. The puckered orthorhombic crystal structure of BP gives rise to asymmetric electronic and phonon dispersion relations: electronic bands are more dispersive along the armchair direction than along the zigzag direction, whereas the phonon dispersion is more dispersive along the zigzag direction.[2,10,11] Along the armchair direction, carriers are more mobile, as the effective mass along the zigzag direction is about 10 times larger than that of along the armchair direction.[12,13] Similarly, the Hall mobility along the armchair direction is 1.8 times the mobility along the zigzag direction .[4] Single and few layers BP absorb light (ranging from infrared to part of the visible spectrum) polarized along the armchair axis, whereas they are transparent for polarization along the zigzag direction.[2] Recent photoluminescence measurements on the monolayer show the existence of anisotropic excitons emitting light, polarized along the armchair direction, with a relatively higher exciton binding energy of

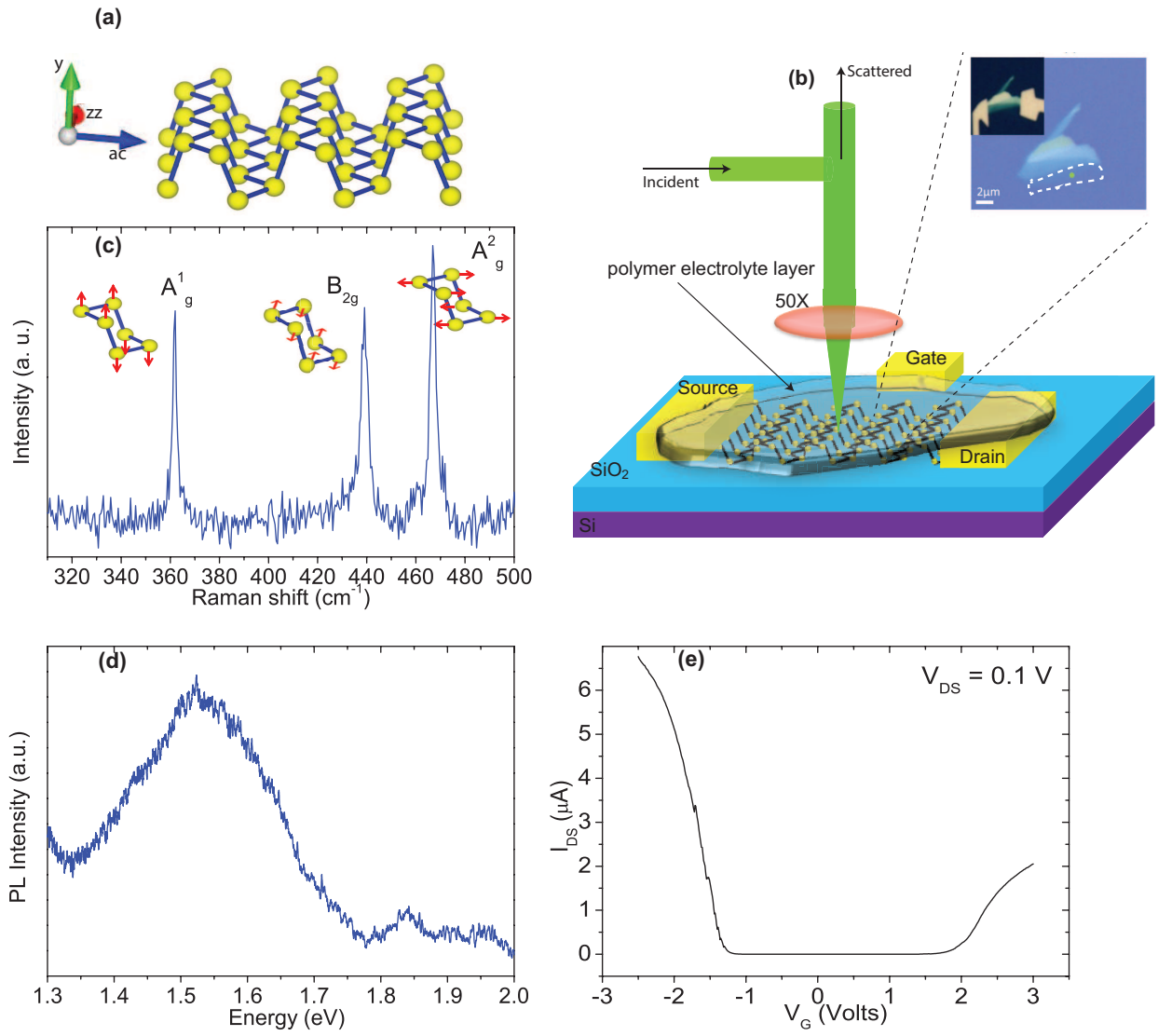

Figure 1: (a) Crystal structure of monolayer BP showing the armchair (ac) and zigzag (zz) directions. (b) A schematic of the experimental set-up, with inset showing optical image of the BP flake and the monolayer region is marked by a dashed line. (c) Raman and (d) photoluminescence spectra recorded from the area dashed line. Laser wavelength used to record spectra is 532 nm. Inset of (c) shows the atomic displacements in normal modes. (e) Transport characteristics of the BP device.

around 0.7-0.8 eV and a quasi particle gap of 2.2 eV.[5,6,14,15]

For 2-D systems like graphene, electron-phonon coupling (EPC) plays a dominant role in the resistivity behaviour at high carrier densities.[16] For almost a decade, since the emergence of graphene,[17,18] Raman spectroscopy has scored over other techniques as an indispensable analytical

tool for estimation of the number of layers in 2D materials like graphene and TMDs,[19–23] to characterize EPC in 2-D graphene [24–26] and evaluating thermal conductivity of graphene layers[27–29] among various other properties. *In-situ* Raman scattering from monolayer MoS_2 transistor have revealed the effect of doping on the EPC strength.[30]

For BP too, Raman spectroscopy has shown its potential as a successful and noninvasive technique to determine the crystal orientation of black phosphorus flakes.[4,5,31,32] Recently Luo *et. al.*[33] have reported anisotropic thermal conductivity using Raman spectroscopy: the thermal conductivity along the zigzag orientation exceeding that along the armchair direction by a factor of 2. The degradation of BP flakes due to environmental aspects have been probed by Raman spectroscopy.[34] With four atoms in the unit cell, out of nine optical modes, phosphorene has six Raman active modes, out of which three prominent modes with irreducible representations ${A^1}_g$, ${A^2}_g$ and B_{2g} are observed in back scattering geometry. The eigen-vectors of these modes reveal that (Figure 1c) ${A^1}_g$ mode involves out of plane displacements of atoms, while the atomic motions involved in ${A^2}_g$ and B_{2g} modes are along armchair and zigzag directions, respectively.

We identify and quantify the effects of doping on the Raman active phonons in phosphorene, revealing characteristic EPC. While ${A^1}_g$ and ${A^2}_g$ phonons are affected by the doping, B_{2g} mode is not. Further ${A^1}_g$, ${A^2}_g$ modes are soften and their linewidths broaden with electron doping while remaining unaffected by holes. Experimental results are supported by first-principle density functional theory (DFT) calculations, which show an enhanced (reduced) EPC for ${A^1}_g$ and ${A^2}_g$ modes with electron (hole) doping. We note that this is consistent with recent reports,[35,36] which suggest a possibility of phosphorene to be a BCS superconductor by virtue of its enhanced EPC at high concentration of electron doping and strain .

Experimental Results and Discussions

Black phosphorus flakes were exfoliated from its single crystal (M/s Smart Elements), and transferred on to a 300 nm SiO_2 grown thermally on a heavily doped Si (M/s Nova Electronic Materials).

Immediately after exfoliation, the substrate was coated with a bilayer resist consisting of PMMA 450K/PMMA 950K to avoid degradation of black phosphorus flakes.[34] After careful observation under a microscope, flakes were selected and photoluminescence (PL) measurement were done to confirm the layer thickness. Figure 1b shows the optical image of the selected flake. Raman spectrum showing the characteristic modes (namely A^1_g, B_{2g} and A^2_g) and PL, recorded from the area marked by dashed line (Figure 1b) are shown in Figure 1c and d respectively. The observed PL peak at $\sim$ 1.53 eV confirms the marked portion to be a single layer phosphorene.[4] Source, drain and gate electrodes were fabricated by e-beam lithography followed by thermal evaporation of 5 nm/70 nm of Cr/Au and lift-off in acetone. A transparent solid polymer electrolyte gate consisting of lithium perchlorate ($LiClO_4$):polyethylene oxide (PEO) in the weight ratio of 1:8 is immediately drop casted to prevent the flake exposure. Due to the nanometer thick ($\sim$2 nm) Debye layer, this polymer electrolyte enables doping with higher carrier concentration (almost by an order of magnitude) as compared to 300 nm oxide gating.[26] Confocal Raman and PL measurements using 532 nm excitation laser are carried out at room temperature using Labram HR-800 coupled with a Peltier cooled CCD and a spectrometer with 1800 lines/mm grating. Spectra are recorded using a long working distance 50X objective with numerical aperture 0.45. Spectra shown in Figure 2 were acquired for 10 seconds using a laser power of $\sim$ 300 μW. Electrical measurements are done using Keithley 2400 source meters. Figure 1b shows the schematic of the experimental set up and the inset shows the device. The device transfer characteristic is shown in Figure 1e displaying an on-off ratio of $\sim 10^5$ and a field effect mobility $\sim$ 100 cm^2/V-sec and $\sim$ 35 cm^2/V-sec for holes and electrons respectively. Similar asymmetric transfer characteristic curves were reported for the BP field effect transistors.[9,37–39] In order to convert the applied gate voltage to carrier concentration n, we have used the standard MOSFET expression $n = C_G\ (V_G - V_T)$, where C_G, V_G and V_T are top gate capacitance, applied top gate voltage and threshold voltage respectively, and C_G is taken to be 1.5μF/cm^2 .[40] It may be noted that the threshold voltage could be different for an isolated monolayer device and can introduce some errors in estimating n. However, the qualitative picture and the interpretation of the results would remain unaffected.

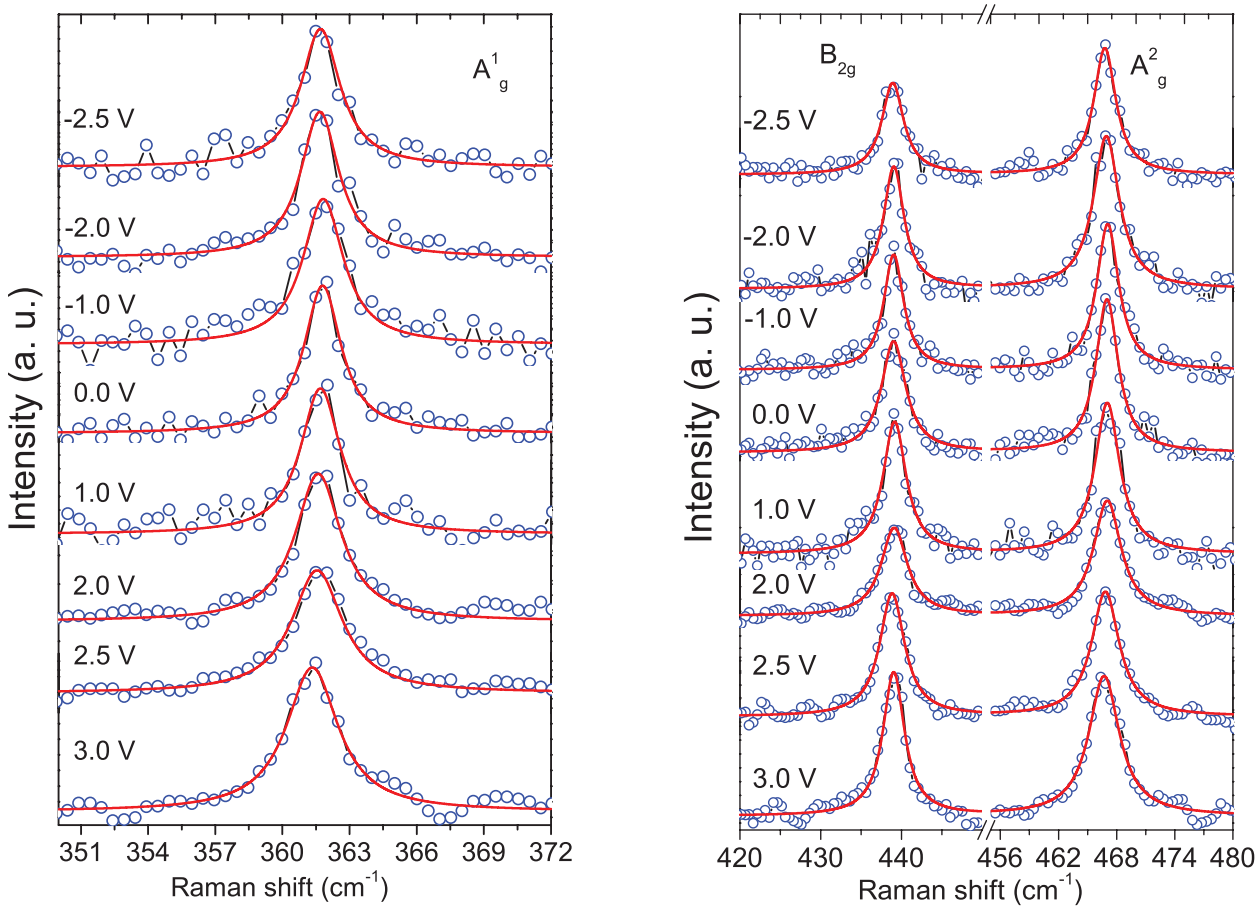

Figure 2: Raman spectra showing (a) A^1_g and (b) B_{2g} and A^2_g modes for different top gate voltages. The top gate voltages are indicated in the figures. Circles are experimental data and lines are Lorentzian fit to the spectrum. The spectra were recorded from the spot marked by green dot in figure 1b.

Figure 2 shows the evolution of the Raman modes of phosphorene as a function of gate voltage V_G. The peak positions and the full width at half maximum (FWHM) are obtained by fitting Lorentzian function (solid lines in Figure 2) to the spectra. The changes in phonon energy $\Delta\omega = \omega(n \neq 0) - \omega(n=0)$ are depicted in Figure 3a, b and c. It can be seen that phonon softening is observed only for the A^1_g and A^2_g modes for electron doping(Figure 3 a, b). Hole doping has no effect on the phonon frequencies. As can be seen in Figure 3c, the B_{2g} mode is not affected by either electron or hole doping. Figure 3d-f show FWHM of the three modes. The FWHM of A^1_g and A^2_g modes increase for the electron doping and do not change for the hole doping. The B_{2g} linewidth does not show any significant doping dependence. Similar phonon and linewidth trends

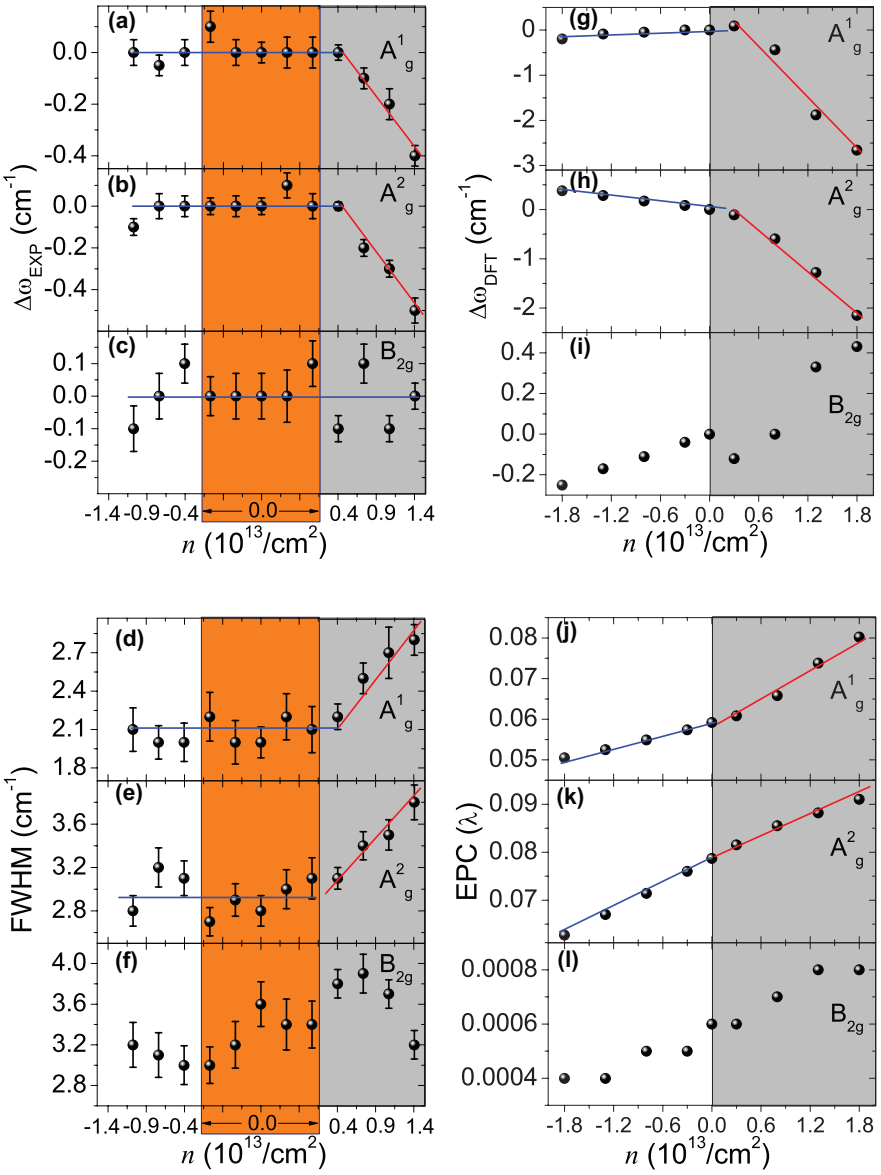

Figure 3: (a) - (c) Changes in phonon frequencies $\Delta\omega$, and (d)- (f) FWHM of Raman peaks, as obtained from experiment, as a function of carrier concentration n. (g) - (i) $\Delta\omega$ obtained from DFT calculations and (j) - (l) calculated values of EPC (λ) as a function of n. The lines are guide to eye. The off-state and electron doped regions are marked with orange and grey shades.

are observed for multilayer BP device (see Supplementary Information). We will now compare our results with the DFT calculations.

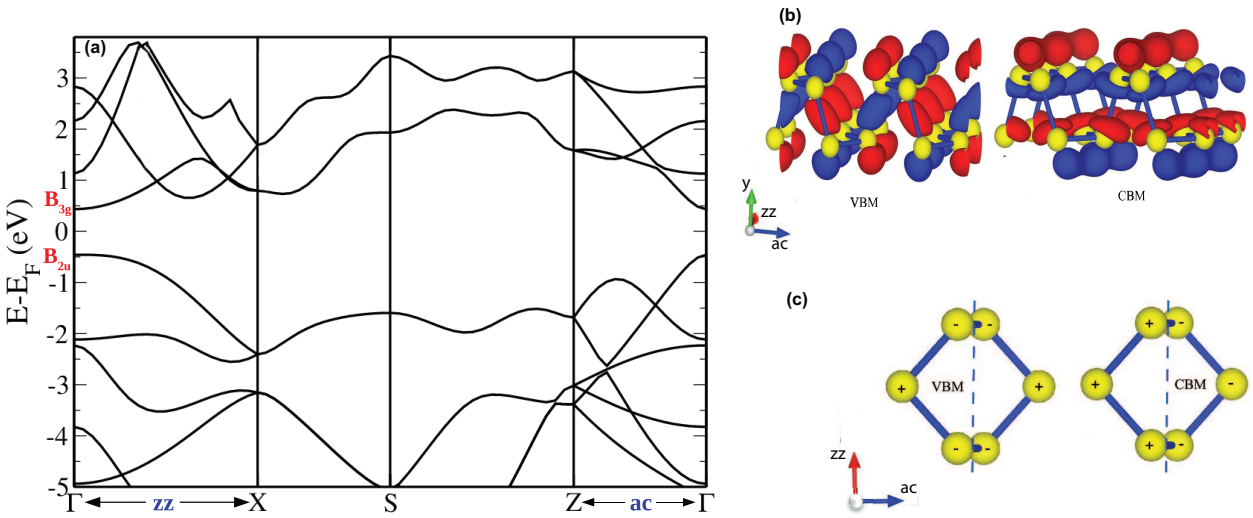

Figure 4: (a) Electronic structure of phosphorene with symmetry labels B_{2u} at VBM (valance band maximum) and B_{3g} at CBM (conduction band minimum) at Γ-point, (b) isosurfaces of wavefunctions at VBM and CBM at the Γ-point, and (c) a schematic showing the symmetry of the wavefuctions at VBM and CBM at Γ-point where dashed line shows a mirror plane. Note that wavefuctions at VBM and CBM are even and odd respectively, under mirror reflection σ_{ac}.

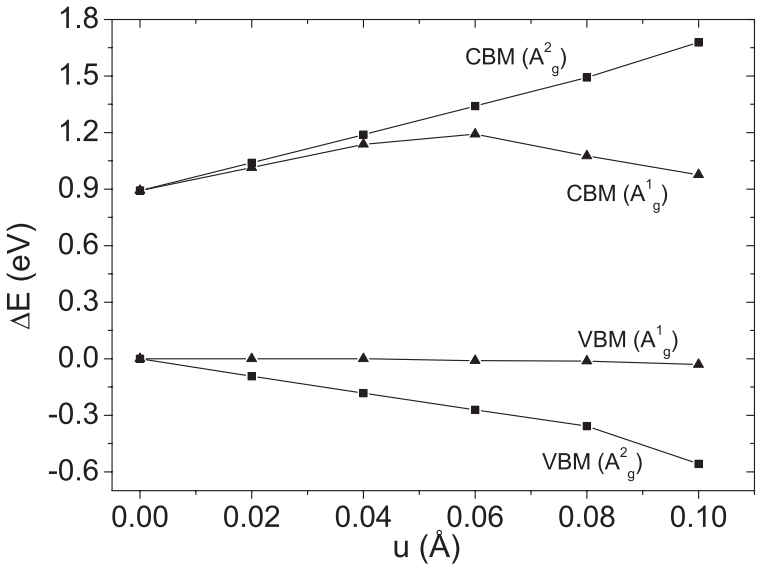

Figure 5: Change in the energies of CBM and VBM as a function of structural distortion obtained by freezing in the atomic displacements of A_g^1 and A_g^2 modes.

Theoretical Calculations

Our first-principles calculations are based on density functional theory as implemented in Quantum ESPRESSO package,[41] and norm-conserving pseudopotentials[42,43] to model the interaction

between valence electrons and ionic cores. The exchange-correlation energy functional is treated within a Local Density Approximation (LDA) with a parametrized form of Perdew and Zunger.[44] We use an energy cutoff of 60 Ry to truncate plane wave basis used in representing Kohn-Sham wave functions, and an energy cutoff of 240 Ry to represent charge density. Structures are relaxed till the Hellman-Feynman force on each atom is less than 0.03 eV/Å. We have used a periodic supercell to simulate a phosphorene sheet, with a vacuum of 15 Å (along y-direction) to separate its adjacent periodic images. Integrations over the Brillouin Zone (BZ) are sampled on 12x1x9 and 48x1x36 uniform meshes of k-points in the calculation of total energy and electron-phonon coupling respectively. For a few concentrations of hole doping (1.3 x 10^{13} cm^{-2} and 1.8 x 10^{13} cm^{-2}), we used 72x1x54 uniform mesh of k-points in the determination of electron-phonon coupling to ensure convergence.

Electronic structure of phosphorene (single layer BP) determined from our first-principles calculations exhibits a direct band gap of 0.89 eV (Figure 4a) at the Γ point, in good agreement with earlier theoretical results.[1] We note that the electronic structure is remarkably different along zigzag (ΓX) and armchair (ΓZ) directions: linear dispersion along the armchair (ac) and parabolic dispersion along zigzag (zz) directions. Electronic states at conduction band minimum (CBM) and valance band maximum (VBM) at Γ point consist of p_y orbitals of phosphorous (Figure 4b). We note that symmetries of the wavefunctions at CBM and VBM are distinct (see Figure 4c), which lead to contrasting effects of electron and hole doping on the electron-phonon coupling (to be explained later).

We have simulated carrier (electron and hole) doping in phosphorene by adding a small fraction of electrons/holes (according to doping concentration) to the unit cell. From the changes in frequencies of the A_g^1 and A_g^2 modes (Figure 3g-i), it is clear that A_g^1 and A_g^2 modes soften significantly with electron doping ($A_g^1 \sim 3$ cm^{-1} and $A_g^2 \sim 2$ cm^{-1} at 1.8×10^{13} cm^{-2}) as compared to insignificant change with hole doping. In contrast, B_{2g} is much less affected by doping. These results are in qualitative agreement with our experimental observations (see Figure 3a-c). To understand these trends, we systematically determined electron-phonon coupling with carrier doping.

The electron-phonon coupling (EPC) of a phonon mode ν at wavevector q (frequeccy ω) is [30,45]

$$\begin{aligned}\lambda_{q\nu} &= \frac{2}{\hbar\omega_{q\nu}N(\varepsilon_F)}\sum_k\sum_{ij}|g^{q\nu,ij}_{k+q,k}|^2\times\delta(\varepsilon_{k+q,i}-\varepsilon_F)\\ &\times \delta(\varepsilon_{k,j}-\varepsilon_F),\end{aligned} \tag{1}$$

where N(ε_F) is the density of states at Fermi energy. The electron-phonon coupling matrix element is

$$g^{q\nu,ij}_{k+q,k} = \left(\frac{\hbar}{2M\omega_{q\nu}}\right)^{\frac{1}{2}}\langle\psi_{k+q,i}|\triangle V_{q\nu}|\psi_{k,j}\rangle, \tag{2}$$

where $\psi_{k,j}$ is electronic wavefunction of j^{th} band at wavevector k, M is the effective mass associated with the phonon, and $\triangle V_{q\nu} = \frac{\partial V}{\partial u^{\nu}(q)}$ is the change in the self-consistent potential associated with atomic displacements of phonon qν.

From calculated λ for all the Raman modes as a function of carrier concentration (Figure 3j-l), it is seen that (a) A_g^1 and A_g^2 modes couple more strongly with the carriers than the B_{2g} mode, and (b) all the modes couple more strongly with electrons than with holes. These results are indeed consistent with our experiments. Strong coupling of the A_g^1 mode with electrons can be understood from symmetry arguments. A_g modes (see Figure 1c) have the full symmetry of the lattice, (*i.e.* distortion along these modes does not break the symmetry of the lattice) and hence all the electronic states (i = j) have a non-zero matrix element (Eq.2). Using the same argument, matrix element (i = j in Eq.2) vanishes for the B_{2g} mode which breaks the symmetry of the lattice (B_{2g} mode is orthogonal to the A_g modes). We do find an asymmetry in the EPC with hole and electron doping: EPC increases with increasing concentration of electron doping while it decreases with increasing hole concentration. This asymmetry follows from the symmetry of the electronic wavefunctions at the VBM and CBM at Γ point. At the VBM, wavefunction is even under mirror reflection, while it is odd at the CBM. As a result, the magnitude as well as the sign of the coupling matrix (Eq.2) can be different for electron and hole doping. It is evident in Figure 3g-h and 3j-k that A_g^1

mode is affected more strongly by electron doping than the hole doping. In contrast, A_g^2 mode is affected by both electron as well as by hole doping, though the effect is stronger for electrons. To understand this, we obtained the energies of VBM and CBM at Γ point as a function of structural distortions obtained by freezing the eigenvectors of these modes. It is evident (Figure 5) that the CBM varies more strongly than the VBM with A_g^1 mode, whereas freezing of A_g^2 mode (Figure5) affects both VBM and CBM significantly, though its effect on the CBM is slightly stronger than that on the VBM. Therefore, the difference in the dependence of A_g^1 and A_g^2 modes on electron and hole doping originates from the matrix element $\langle \psi_{k,i} | \Delta V_{qv} | \psi_{k,j} \rangle$. The non-monotonous evolution of CBM as a function of distortion for A_g^1 mode is further explained in the supplementary material.

We note that low levels of doping results in changes in the population of only the states that have energies close to the VBM and CBM at Γ point. Thus, the states lining the band-gap along Γ-X direction are more relevant to our experiments than the ones along Γ-Z (energies of the states at Z-point are too far (Fig. 4a) from the gap to be affected by low levels of doping in phosphorene transistor). In Fig. S5a, we have shown iso-surfaces of wavefunctions of the valence and conduction bands at X-point and a diagram of their projections on p-orbitals of P. We note that the bands at X point are doubly degenerate, and are made from p_x and p_y orbitals of P, in contrast to the VBM and CBM at Γ point made from p_y orbitals. From the Fig. S5b, it is clear that the relative phases of p orbitals of the P sublattices are the same for wave functions at X and Γ (Fig. 4c) points. Hence, our symmetry analysis of the coupling of Raman active phonons to the states along Γ to X is similar. Since the orbitals involved in the VBM and CBM bands at X point are different from those at Γ point, their relative phase factors are not simple. In fact, they involve rotations in the 3-dimensional space of bands made of two p-orbitals. Thus, their relative phases can be meaningfully described with a Hermitian matrix that is responsible for the complex Raman tensor relevant to the polarization dependent Raman scattering.[32] To connect more closely with the results of reference 32, we determined optical dielectric constants of structures obtained by freezing A_g^1 and A_g^2 modes. $\Delta\varepsilon_{xx}$ and $\Delta\varepsilon_{zz}$ are 0.05 and 1.3 for A_g^1 and 0.2 and 1.5 for A_g^2 modes, respectively. This confirms a remarkable anisotropy in the Raman tensor, quite distinct for A_g^1 and A_g^2 modes,

in qualitative agreement with the fitted parameters obtained from polarization dependent Raman spectra of Phosphorene.[32]

Conclusions

Our work demonstrates a phosphorene-based field effect transistor (P-FET) with a high on-off ratio, in which the carrier concentration in phosphorene channel can be effectively controlled by the top-gate electrode. We have shown how *in-situ* Raman spectroscopy can be a powerful tool in assessing the nature and concentration of carriers in the channel of P-FET. While the anisotropy in its properties is expected from its structural symmetry, we uncover a remarkable electron-hole asymmetry in the coupling between its charge carriers and phonons: phonons with A_g symmetry couple much more strongly with electrons than with holes. Further, only the phonons preserving the symmetry of the lattice couple strongly with electrons. Our first-principles calculations reveal that the electron-hole asymmetry arises from rather different characters of conduction and valence bands involving π and σ bonding states respectively.

The angular dependence of the intensities of A_g^1, A_g^2 and B2g phonons in black phosphorus (BP) has been recently well studied.[32] It is shown that for reproducing experimental results for intensities of Ag modes, the Raman tensor has to be complex whereas for B_{2g}, real values of Raman tensor elements can explain the angular dependence. The complex values of the Raman tensor can arise both from electron-radiation as well as electron-phonon matrix elements. An interesting aspect brought out is that the imaginary part of the Raman tensor elements is different for the two totally symmetric modes A_g^1 and A_g^2 , pointing out that electron-phonon interaction is a key factor responsible for the complex values of the tensor. In our work, we have shown that electron-phonon coupling (EPC) associated with A_g^1 and A_g^2 modes vary predominantly with electron doping. Our experiments did not focus on the angular dependence of the Raman intensities. The work of Ref. 32 by Ribeiro et.al. points out an interesting future possibility to study the angular dependence of Raman intensities of A_g modes as a function of carrier concentration and see how the relative

phase factor (i.e. the imaginary part of the Raman tensor elements) for the A_g mode varies. This will further quantify the contribution of electron-phonon matrix elements to the real and imaginary parts of the Raman tensor elements. Our work is fundamental to understanding the transport in phosphorene and key to measurement of carriers in phosphorene-based nanoelectronic devices.

Acknowledgement

BC, AKS, and UVW thank the financial support under the Nano Mission project of the Department of Science and Technology, Government of India. AD thanks IISc start up grant for the financial support.

References

(1) Liu, H.; Neal, A. T.; Zhu, Z.; Luo, Z.; Xu, X.; Tománek, D.; Ye, P. D. *ACS Nano* **2014**, *8*, 4033–4041.

(2) Tran, V.; Soklaski, R.; Liang, Y.; Yang, L. *Phys. Rev. B* **2014**, *89*, 235319.

(3) Castellanos-Gomez, A.; Vicarelli, L.; Prada, E.; Island, J. O.; Narasimha-Acharya, K.; Blanter, S. I.; Groenendijk, D. J.; Buscema, M.; Steele, G. A.; Alvarez, J.; Zandbergen, H. W.; Palacios, J.; van der Zant, H. S. J. *2D Materials* **2014**, *1*, 025001.

(4) Xia, F.; Wang, H.; Jia, Y. *Nature Communications* **2014**, *5*, 4458.

(5) Wang, X.; Jones, A. M.; Seyler, K. L.; Tran, V.; Jia, Y.; Zhao, H.; Wang, H.; Yang, L.; Xu, X.; Xia, F. *Nature Nanotechnology* **2015**, *10*, 517–521.

(6) Yang, J.; Xu, R.; Pei, J.; Myint, Y. W.; Wang, F.; Wang, Z.; Zhang, S.; Yu, Z.; Lu, Y. *Light:Science and Application* **2015**, *4*.

(7) Liang, L.; Wang, J.; Lin, W.; Sumpter, B. G.; Meunier, V.; Pan, M. *Nano Letters* **2014**, *14*, 6400–6406.

(8) Buscema, M.; Groenendijk, D. J.; Steele, G. A.; van der Zant, H. S.; Castellanos-Gomez, A. *Nature Communications* **2014**, *5*, 4651.

(9) Li, L.; Yu, Y.; Ye, G. J.; Ge, Q.; Ou, X.; Wu, H.; Feng, D.; Chen, X. H.; Zhang, Y. *Nature Nanotechnology* **2014**, *9*, 372–377.

(10) Fei, R.; Yang, L. *Applied Physics Letters* **2014**, *105*, 083120.

(11) Cai, Y.; Ke, Q.; Zhang, G.; Feng, Y. P.; Shenoy, V. B.; Zhang, Y.-W. *Advanced Functional Materials* **2015**, *25*, 2230–2236.

(12) Akahama, Y.; Endo, S.; Narita, S.-i. *Journal of the Physical Society of Japan* **1983**, *52*, 2148–2155.

(13) Ling, X.; Wang, H.; Huang, S.; Xia, F.; Dresselhaus, M. S. *Proceedings of the National Academy of Sciences* **2015**, *112*, 4523?4530.

(14) Schuster, R.; Trinckauf, J.; Habenicht, C.; Knupfer, M.; Büchner, B. *Phys. Rev. Lett.* **2015**, *115*, 026404.

(15) Rodin, A. S.; Carvalho, A.; Castro Neto, A. H. *Phys. Rev. B* **2014**, *90*, 075429.

(16) Efetov, D. K.; Kim, P. *Phys. Rev. Lett.* **2010**, *105*, 256805.

(17) Novoselov, K. S.; Geim, A. K.; Morozov, S.; Jiang, D.; Zhang, Y.; Dubonos, S.; Grigorieva, I.; Firsov, A. *science* **2004**, *306*, 666–669.

(18) Geim, A. K.; Novoselov, K. S. *Nature Materials* **2007**, *6*, 183–191.

(19) Ferrari, A. C.; Meyer, J. C.; Scardaci, V.; Casiraghi, C.; Lazzeri, M.; Mauri, F.; Piscanec, S.; Jiang, D.; Novoselov, K. S.; Roth, S.; Geim, A. K. *Phys. Rev. Lett.* **2006**, *97*, 187401.

(20) Gupta, A.; Chen, G.; Joshi, P.; Tadigadapa, S.; Eklund, P. *Nano Letters* **2006**, *6*, 2667–2673.

(21) Graf, D.; Molitor, F.; Ensslin, K.; Stampfer, C.; Jungen, A.; Hierold, C.; Wirtz, L. *Nano Letters* **2007**, *7*, 238–242.

(22) Lee, C.; Yan, H.; Brus, L. E.; Heinz, T. F.; Hone, J.; Ryu, S. *ACS nano* **2010**, *4*, 2695–2700.

(23) Berkdemir, A.; Gutiérrez, H. R.; Botello-Méndez, A. R.; Perea-López, N.; Elías, A. L.; Chia, C.-I.; Wang, B.; Crespi, V. H.; López-Urías, F.; Charlier, J.-C.; Terrones, H.; Terrones, M. *Scientific reports* **2013**, *3*.

(24) Pisana, S.; Lazzeri, M.; Casiraghi, C.; Novoselov, K. S.; Geim, A. K.; Ferrari, A. C.; Mauri, F. *Nature Materials* **2007**, *6*, 198–201.

(25) Yan, J.; Zhang, Y.; Kim, P.; Pinczuk, A. *Phys. Rev. Lett.* **2007**, *98*, 166802.

(26) Das, A.; Pisana, S.; Chakraborty, B.; Piscanec, S.; Saha, S.; Waghmare, U.; Novoselov, K.; Krishnamurthy, H.; Geim, A.; Ferrari, A.; Sood, A. *Nature Nanotechnology* **2008**, *3*, 210–215.

(27) Balandin, A. A.; Ghosh, S.; Bao, W.; Calizo, I.; Teweldebrhan, D.; Miao, F.; Lau, C. N. *Nano Letters* **2008**, *8*, 902–907.

(28) Faugeras, C.; Faugeras, B.; Orlita, M.; Potemski, M.; Nair, R. R.; Geim, A. *ACS Nano* **2010**, *4*, 1889–1892.

(29) Lee, J.-U.; Yoon, D.; Kim, H.; Lee, S. W.; Cheong, H. *Phys. Rev. B* **2011**, *83*, 081419.

(30) Chakraborty, B.; Bera, A.; Muthu, D. V. S.; Bhowmick, S.; Waghmare, U. V.; Sood, A. K. *Phys. Rev. B* **2012**, *85*, 161403.

(31) Wu, J.; Mao, N.; Xie, L.; Xu, H.; Zhang, J. *Angewandte Chemie 54*, 2366–2369.

(32) Ribeiro, H. B.; Pimenta, M. A.; de Matos, C. J.; Moreira, R. L.; Rodin, A. S.; Zapata, J. D.; de Souza, E. A.; Castro Neto, A. H. *ACS Nano* **2015**, *9*, 4270?4276.

(33) Luo, Z.; Maassen, J.; Deng, Y.; Du, Y.; Lundstrom, M. S.; Ye, P. D.; Xu, X. *Nature Communications* **2015**,

(34) Favron, A.; Gaufrès, E.; Fossard, F.; Phaneuf-L?Heureux, A.-L.; Tang, N. Y.; Lévesque, P. L.; Loiseau, A.; Leonelli, R.; Francoeur, S.; Martel, R. *Nature Materials* **2015**, *14*, 826–832.

(35) Ge, Y.; Wan, W.; Yang, F.; Yao, Y. *New Journal of Physics* **2015**, *17*, 035008.

(36) Shao, D.; Lu, W.; Lv, H.; Sun, Y. *EPL (Europhysics Letters)* **2014**, *108*, 67004.

(37) Koenig, S. P.; Doganov, R. A.; Schmidt, H.; Neto, A. C.; Oezyilmaz, B. *Applied Physics Letters* **2014**, *104*, 103106.

(38) Das, S.; Zhang, W.; Demarteau, M.; Hoffmann, A.; Dubey, M.; Roelofs, A. *Nano Letters* **2014**, *14*, 5733–5739.

(39) Cao, Y. et al. *Nano Letters* **2015**, *15*, 4914–4921.

(40) Chakraborty, B.; Das, A.; Sood, A. *Nanotechnology* **2009**, *20*, 365203.

(41) Giannozzi, P. et al. *J. Phys.: Condens. Matter* **2009**, *21*, 395502.

(42) Hartwigsen, C.; Goedecker, S.; Hutter, J. *Phys. Rev. B* **1998**, *58*, 3641–3662.

(43) Goedecker, S.; Teter, M.; Hutter, J. *Phys. Rev. B* **1996**, *54*, 1703–1710.

(44) Perdew, J. P.; Zunger, A. *Phys. Rev. B* **1981**, *23*, 5048–5079.

(45) Attaccalite, C.; Wirtz, L.; Lazzeri, M.; Mauri, F.; Rubio, A. *Nano Letters* **2010**, *10*, 1172–1176.

SUPPLEMENTARY INFORMATION

Electron-Hole Asymmetry in the Electron-phonon Coupling in Top-gated Phosphorene Transistor

Experimental Results for the Multilayer BP

We observe similar trends for A_g and B_{2g} modes for a top-gated multilayer BP ($\sim$ 9 layers) device. The transfer characteristics are shown in figure SF6. The field effect mobilities were estimated to be 40 cm^2/V-sec and 25 cm^2/V-sec for holes and electrons, respectively. Raman spectra showing the evolution of different modes at different top gate voltages are shown in figure SF7 a and b. The frequency and linewidth pattern are similar to what we have demonstrated for monolayer. For doping with electrons, the ${A^1}_g$ and ${A^2}_g$ modes soften (figure SF8 a and b) while remaining unchanged for hole doping. The FWHM for these modes increase for electron side only (figure SF8 d and e). The B_{2g} mode is not affected by gating as evident from frequency and linewidth trends in figure SF8 c and f, respectively.

Electronic Structure of Phosphorene

Figure SF9 a shows electronic structure of phosphorene calculated using DFT where the conduction bands CBM and CBM+1 are marked. Figure SF9 b shows the isosurfaces of wavefunctions of CBM and CBM+1 with structural distortion of A_g^1 mode for 0.04 Å and 0.06 Å, that reveal the band inversion between CBM and CBM+1 bands. The p_y orbitals get flip by 180^0 s i.e. ψ = -ψ confirming band inversion of CBM and CBM+1. This can be the reason for the non-monotonous dependence of CBM energy on the structural distortion associated with the A_g^1 mode shown in Figure 5 in the main text. This may also be relevant to studies of excited state properties of black phosphorus. Isosurfaces of wavefunctions at VBM and CBM at the X-point along with a schematic

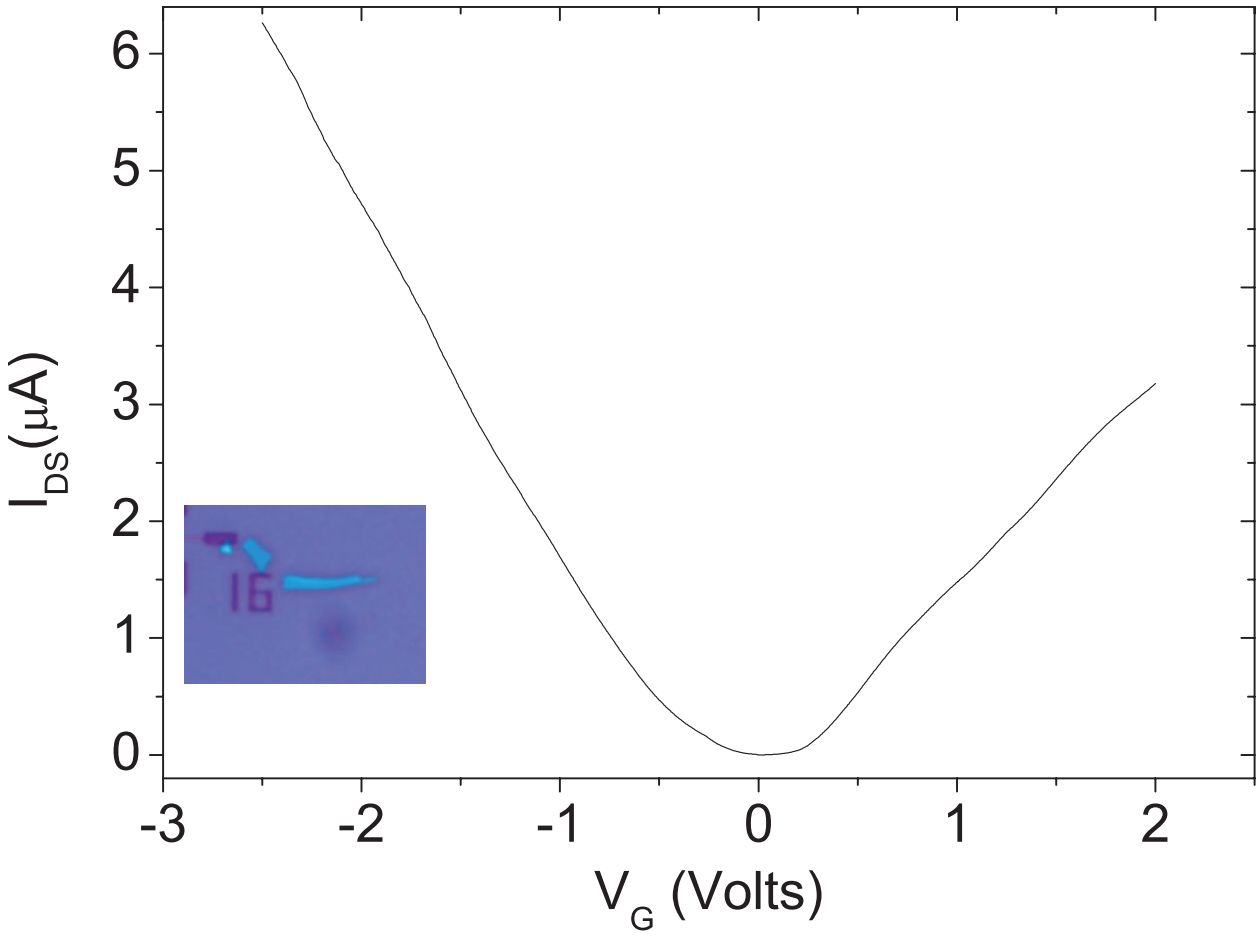

Figure SF6: Multilayer BP transfer characteristic. Drain-source volatge was 0.05 V. Inset shows the multilayer flake.

diagram of projerction on $p_{x,y}$-orbitals of P showing symmetry of the wavefunction at VBM and CBM at X-point are shown in figure SF10.

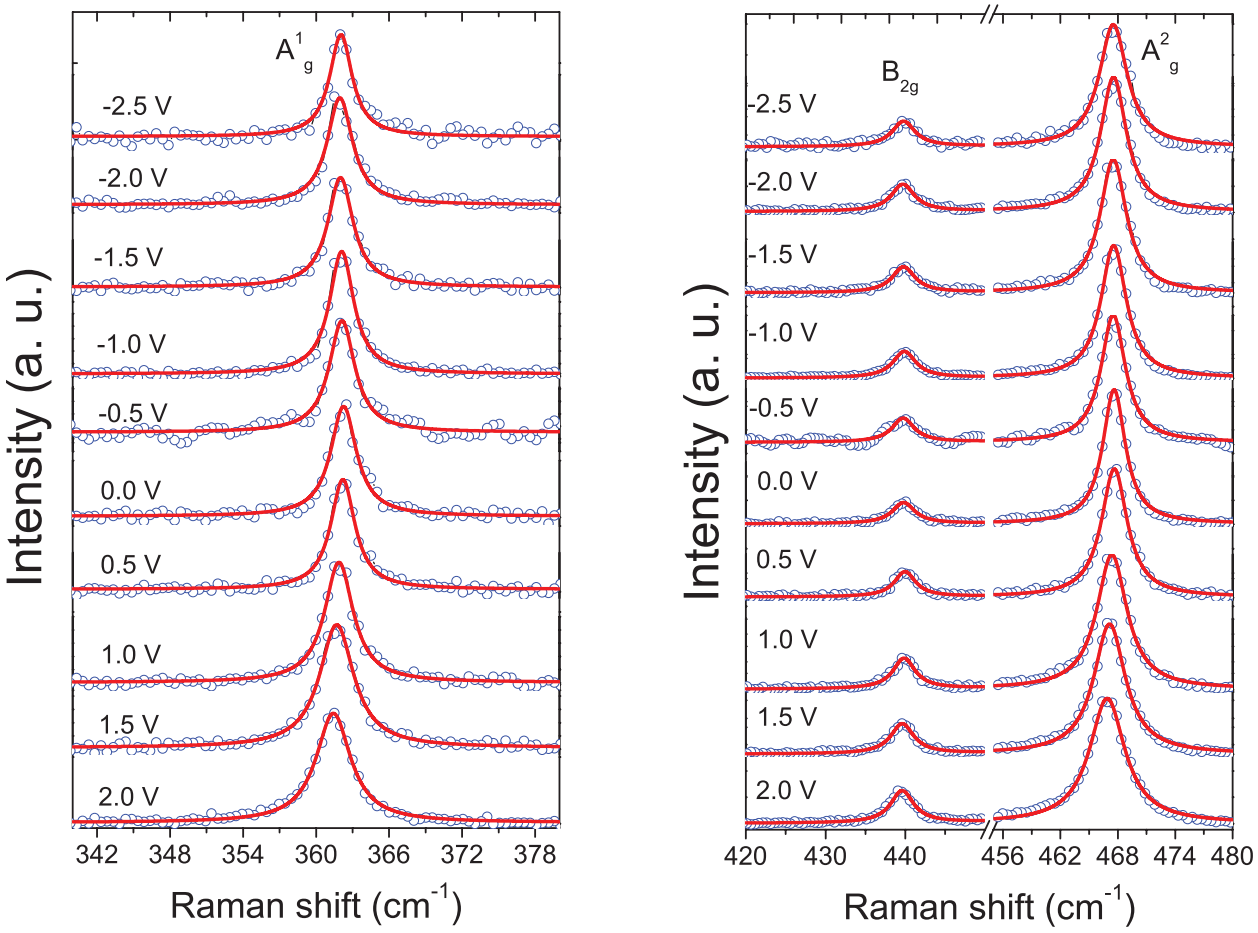

Figure SF7: Raman spectra from multilayer BP showing (a) $A^1{}_g$ and (b) B_{2g} and $A^1{}_g$ modes for different top gate voltages. The top gate voltages are indicated in the figures. Circles are experimental data and lines are Lorentzian fit to the spectrum.

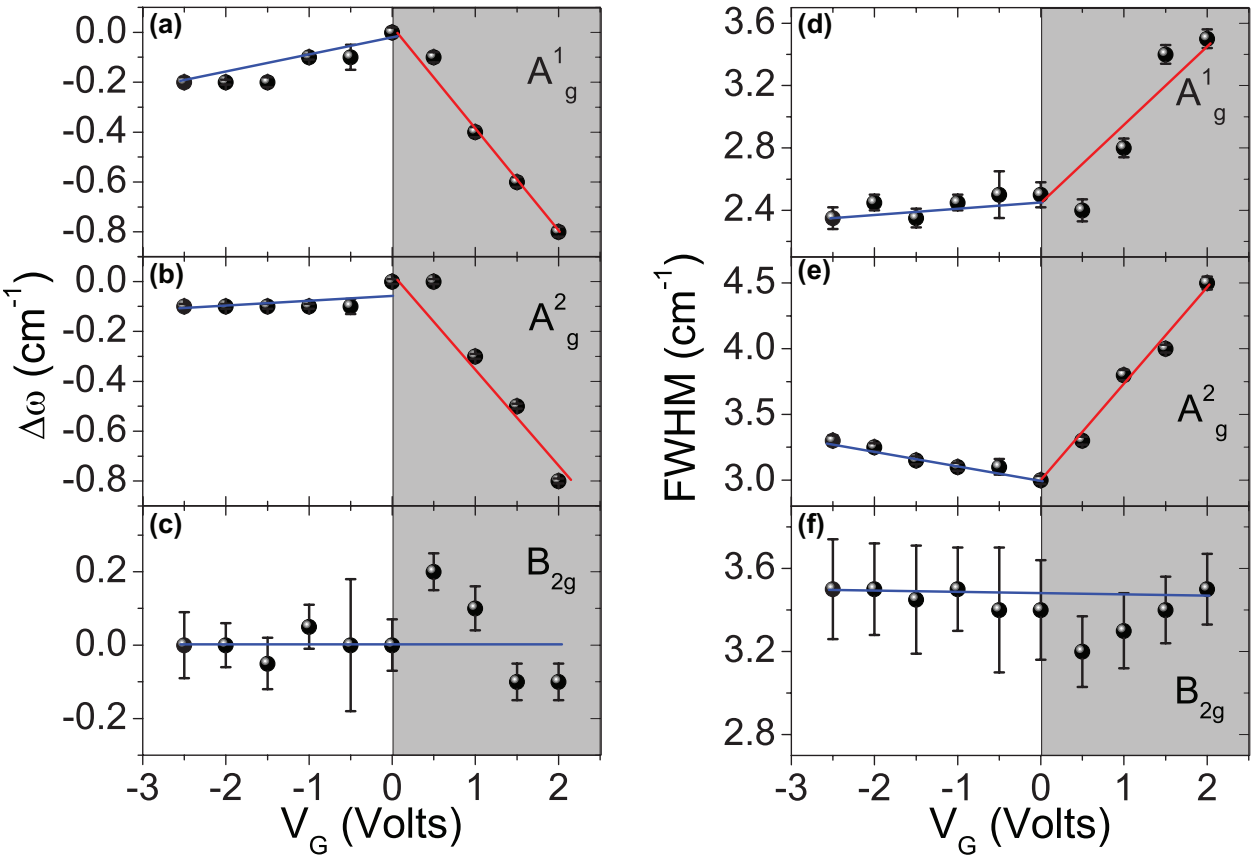

Figure SF8: (a)- (c) Changes in Phonon frequency $\Delta\omega$, as a function of carrier concentration n. (d) - (f) FWHM as a function of n. Electron doped region is shaded. The lines are guide to eye.

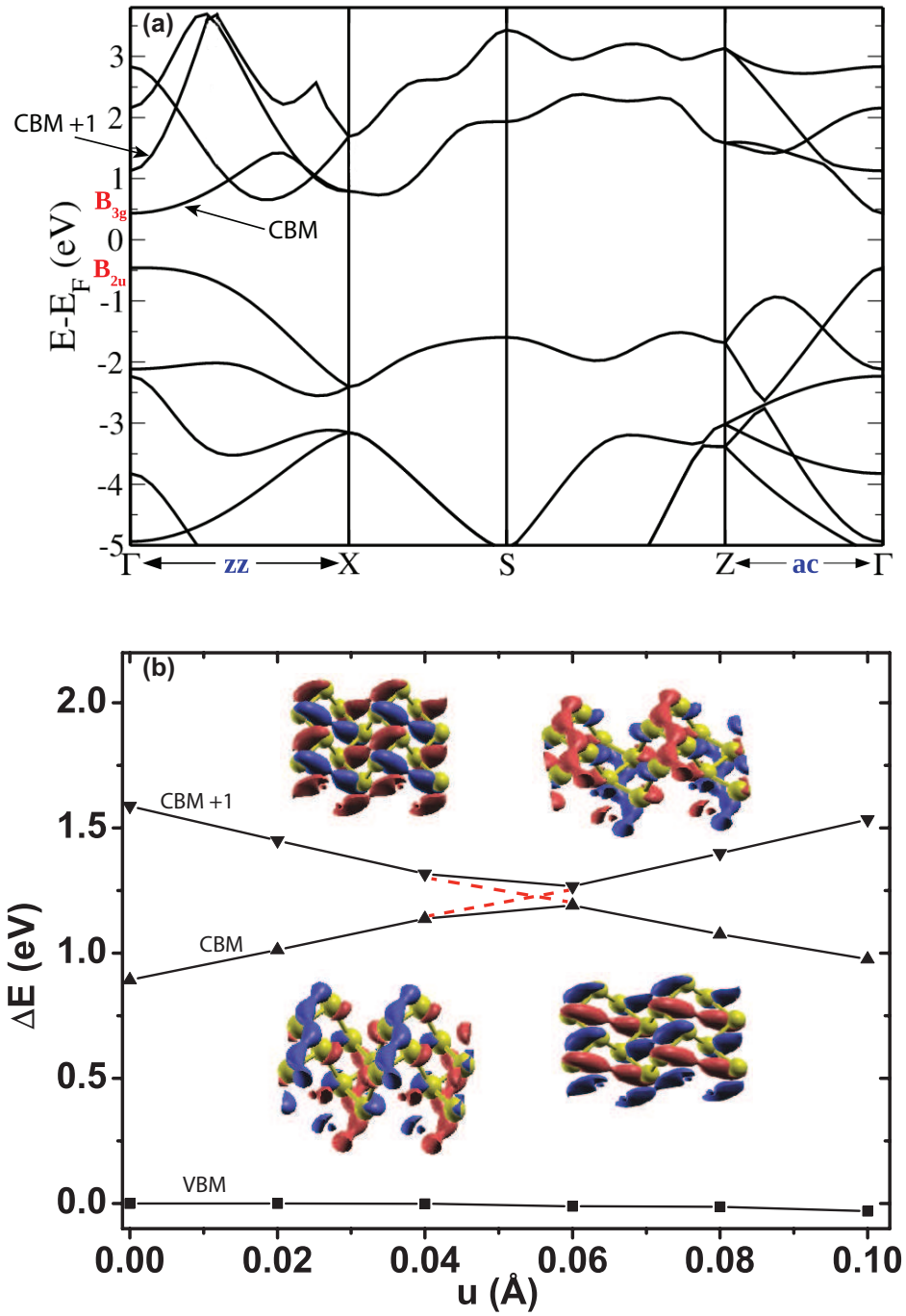

Figure SF9: (a) Electronic structure of phosphorene with CBM and CBM +1 marked. (b) Isosurfaces of wavefunctions of CBM and CBM+1 with structural distortion of A_g^1 mode for 0.04 Å and 0.06 Å, that reveal the band inversion between CBM and CBM+1 bands. If both the p_y orbitals are seen in the same reference frame across the red dashed line, we observe that p_y orbitals get flipped by 180^0 i.e. $\psi = -\psi$ confirms band inversion of CBM and CBM+1.

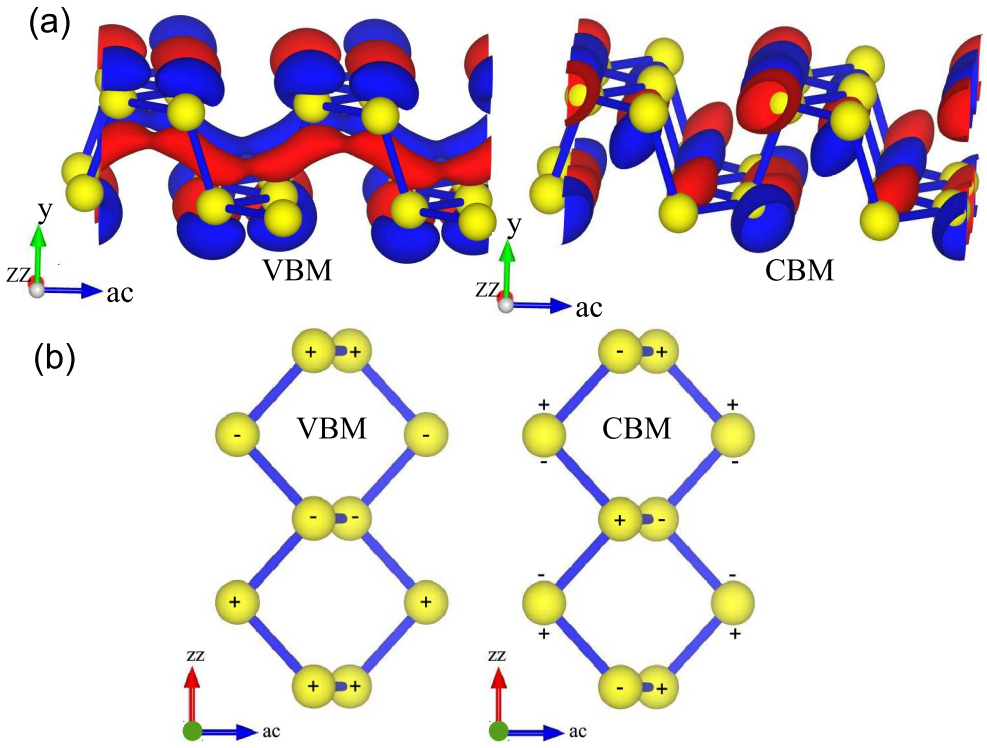

Figure SF10: (a) Isosurfaces of wavefunctions at VBM and CBM at the X-point and (b) a schematic diagram of projection on $p_{x,y}$-orbitals of P showing symmetry of the wavefunction at VBM and CBM at X-point. Note that states at the VBM and CBM at X-point are doubly degenerate and isosurfaces of the degenerate states (VBM and VBM-1 or CBM and CBM+1) are similar.